



Pearlite Spheroidisation and Microstructure Refinement Through Heavy Warm Deformation of Hot Rolled 55VNb Microalloyed Steel

Y. MONTAÑA, Z. IDOYAGA, I. GUTIÉRREZ, and A. IZA-MENDIA

The microstructure evolution of 55VNb microalloyed steel during warm deformation *via* single pass uniaxial compression was researched, and the effect of deformation conditions on dynamic spheroidisation of cementite lamellae and ferrite conditioning for a range of deformation temperatures (600 °C to 700 °C) and strain rates (1 to 10 s⁻¹) analysed. Cementite lamellae appear to subdivide irrespective of deformation temperature with the ferrite phase penetrating the pattern formed by the cementite crystallites, in turn confirming that the dissolution of this phase during deformation is an important mechanism leading to the break-up of plates and subsequent globulisation. EBSD measurements allowed orientation gradients leading to the final subdivision of the cementite to be determined. Ferrite softening during heavy warm deformation is attributed to dynamic recovery and continuous dynamic recrystallisation, although the evolution of this phase depends, to a great extent, on the region subject to study, as confirmed by local EBSD studies. Misorientation profiles obtained in different regions of ferrite and pearlite enabled the different stages of the microstructural evolution to be monitored for each phase, this being developed *via* a variety of mechanisms under the same deformation conditions. Finally, the increase in low angle boundary density correlates with the Zener–Hollomon parameter, and a linear relation between the density of low angle boundaries and steady-state stress estimated for pearlite and ferrite was found, indicating that new boundaries would have been formed dynamically during deformation. High angle boundary density also increases with deformation, although this is almost irrespective of the temperature and strain rate applied.

<https://doi.org/10.1007/s11661-022-06688-0>
© The Author(s) 2022

I. INTRODUCTION

THE aim of spheroidisation treatments applied to medium and high carbon steels is to increase ductility, toughness or cold formability, although expensive thermal treatments are required, involving long holding times (10 to 24 h) at temperatures just (10 °C to 20 °C) below A_{e1} . To reduce or replace these thermal treatments, different strategies have been developed based on the application of advanced thermomechanical processes, including deformation above A_{e1} to induce

deformation-induced divorced eutectic transformation (DET),^[1–4] deformation-induced transformation (DIT)^[5–7] at temperatures close to or below intercritical temperature, or the application of heavy warm deformation (HWD) either directly^[8] or in combination with thermal treatments^[9–12] or coiling.^[13] Additionally, HWD may produce a nanostructured ferrite microstructure, the advantage of which, in combination with a globular cementite microstructure, is the potential increase in strength, ductility and toughness in comparison to a coarse grained and fully pearlitic lamellar microstructure.

As cementite is very hard and brittle in comparison to ferrite, it would be expected not to deform plastically to a significant level, but to behave elastically.^[14] Nevertheless, the deformability of pearlite depends on several factors. Umemoto *et al.*^[15] have reported that when deformed below 300 °C, cementite does not deform plastically and fractures within elastic limit. However, at higher temperatures and low strain rates, plastic deformability of cementite increases and cementite lamellae in deformed pearlite show inhomogeneous slip, thinning by deck-of-cards slip, homogeneous bending,

Y. MONTAÑA, I. GUTIÉRREZ, and A. IZA-MENDIA are with the Ceit, Manuel Lardizabal 15, 20018 Donostia-San Sebastián, Basque Country, Spain and also with Universidad de Navarra, Tecnun, Manuel Lardizabal 13, 20018 Donostia-San Sebastián, Basque Country, Spain. Contact e-mail: aiza@ceit.es Z. IDOYAGA is with the SIDENOR I+D S.A., 48970 Basauri, Basque Country, Spain.

Manuscript submitted August 31, 2021; accepted April 8, 2022.

Article published online May 9, 2022

fragmentation, cleavage fracture and cracking by shear bands. Cementite dissolution is also obtained increasing the temperature and/or applying severe deformation.

In applying a combination of processing maps and microstructural analysis, Rastegari *et al.*^[8] identified dynamic spheroidisation of cementite lamellae as occurring in eutectoid steels at a range of deformation temperatures between 640 °C and 740 °C at low strain rates within the range 0.01 to 0.1 s⁻¹. These can be extended up to 1 s⁻¹ within the range 730 °C to 740 °C. Outside these deformation ranges, microstructural instabilities may occur, leading to flow localisation and resulting in microstructural defects such as lamellar sliding, kinking or cracking and prior austenite grain boundary cracking.

The evolution of a pearlitic or ferrite-pearlitic microstructure during HWD is the result of dynamic recovery and, eventually, continuous dynamic recrystallisation phenomena taking place in ferrite^[16] and of the dynamic spheroidisation of the cementite lamellae. Fragmentation of this phase involves the formation of grooves or kinks that favour local solubility of cementite and encourages the break-up of the lamellae into smaller plates. The carbon diffusion in the vicinity of the plate tips in turn contributes to a steady reduction in the aspect ratio of the lamellar debris to produce spherical shapes.^[8,17,18] These mechanisms are not so different from those reported as occurring statically during spheroidisation treatments but are enhanced by the presence of dislocations in the surrounding ferrite that favours carbon diffusion and accelerates the process,^[17] eventually forming sub-boundaries *via* the deformation effect on the cementite plates.^[18]

The present work applied a heavy warm deformation sequence (HWD) below the γ - α transformation-temperature in order to attain:

- the spheroidisation of cementite in fine and homogeneously distributed particles
- ferrite conditioning (strain accumulation)

By applying high deformation, the aim is to develop an ultrafine grained microstructure in addition to a significant increase in pearlite spheroidisation. As such, determining deformation conditions deemed suitable for producing ultrafine grain microstructures and determining the relationship between variables such as strain, strain rate and deformation temperature, will enable rolling conditions to be applied in future warm caliber rolling trials to be defined accordingly.

Table I. Steel Composition (Weight Percent)

C	Mn	Si	V	Nb
0.53	0.84	0.32	0.13	0.02

II. EXPERIMENTAL

A hot rolled 55VNb steel bar of 90 mm in diameter was produced industrially by Sidenor, with the composition shown in Table I. Uniaxial compression specimens of 10 mm in diameter and 15 mm in height were machined out from the centre of this bar.

Uniaxial compression single pass warm deformation to a true strain of 1 was applied on a Gleeble 3800 at 600 °C and 700 °C and at strain rates of 1 and 10 s⁻¹, followed by water quenching down to room temperature. The resulting samples were sectioned along their longitudinal axis for microstructural characterisation.

Compression tests give rise to a heterogeneous distribution of the resulting deformation through the section of the sample in which the smaller deformation occurs below the area of contact with the tools, while the diagonal and central parts may reach significantly higher local strain levels than the nominal strain applied.^[17]

Optical microscopy was applied after conventional polishing and etching with 2 pct Nital. The mean interlamellar spacing was determined in FEG-SEM micrographs as the reciprocal of N_L , *i.e.*, the number of intersections of cementite lamellae with the circumference of a circular network. The magnification was chosen by taking into account the recommendations set out in the ASTM E-112-96 standard.

Given that warm deformation produces a substructure that is difficult to resolve by optical microscopy, electron backscattered diffraction (EBSD) techniques were applied. The samples were prepared using conventional metallographic methods and a final soft polishing with colloidal silica. Areas of 90 × 90 μm were scanned using a 0.1 μm step size. EDAX-TSL OIM Analysis software package was used to obtain different images from the EBSD scan data obtained as follows: image quality (IQ) maps, boundary maps with different tolerance angles and inverse pole figures. The boundary length density, defined as the boundary line length per unit area (in μm⁻¹), was also determined.

III. RESULTS

The starting microstructure present at the centre of the industrially produced bar is shown in Figure 1(a) and (b). Ferrite grains appear decorating prior austenite grain boundaries and as ferrite idiomorphs nucleated intragranularly on inclusions. The fraction of ferrite is of around 13.5 ± 1.7 pct, the rest of the microstructure being pearlite with an interlamellar spacing of about 0.22 ± 0.03 μm. The EBSD images in Figure 2 show some ferrite grains along a prior austenite grain boundary, with these grains having different orientations and their boundaries being of high angle (misorientation > 15 deg). Within the pearlite, the cementite lamellae are not well defined, although they can be distinguished on the IQ map in Figure 2(a). The pearlite nodules appear surrounded by high angle boundaries (HABs), as shown in Figure 2(b), and low angle boundaries (misorientation between 2 and 15 deg) can be seen

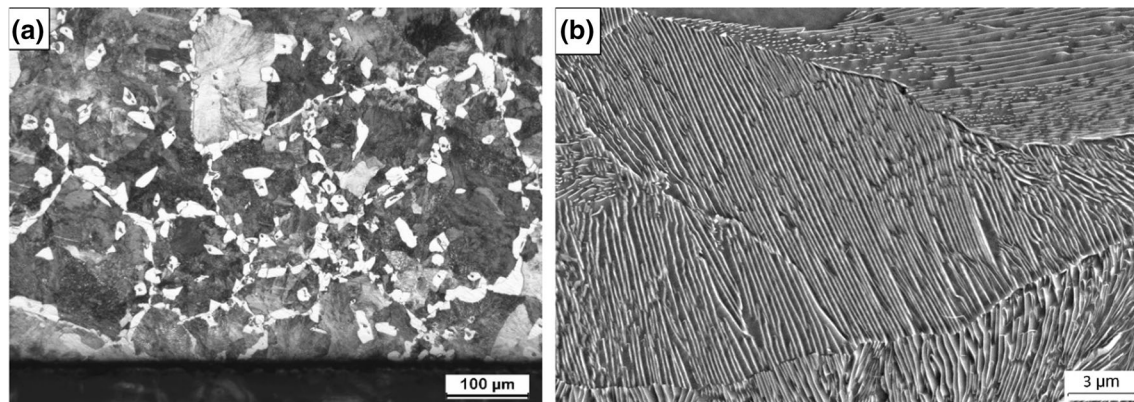


Fig. 1—Microstructure at the centre of the hot rolled bar (a) optical image of the ferrite-pearlite microstructure and (b) FEG-SEM image of the pearlite.

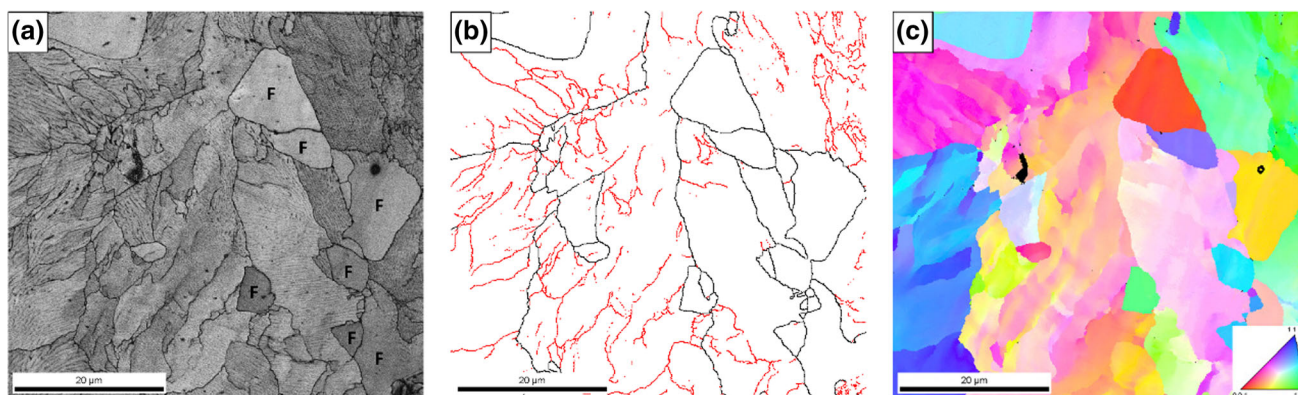


Fig. 2—EBSD images of the microstructure at the centre of the hot rolled bar: (a) IQ map, (b) low 2–15 deg (red) and high >15 deg (black) boundary map and (c) orientation map (Color figure online).

within them, probably associated with the pearlite colonies. The misorientation pattern within the pearlite can be more clearly seen in the orientation map in Figure 2(c). As a result, evidence has been found that, before any deformation is applied, some low angle boundaries (LABs) are already present in the pearlite microstructure. Another aspect to be mentioned is that the texture is almost random prior to deformation, as can be seen in Figure 2(c).

The effect of deformation on the microstructure will be analysed in detail below. First of all, it should be stated that distribution of the deformation in the axially compressed samples is far from being homogenous, as Figure 3 shows, in which three different zones can be identified. The first corresponds to the high strain region (HSR) at the centre of the compressed specimen. As shown in the same figure, in this case, the microstructure appears elongated in the direction perpendicular to the applied stress. The second zone corresponds to a low strain region (LSR) below the tool where the microstructure remains almost equiaxed and appears, on the specimen, both above and below the HSR. The third zone corresponds to the specimen diagonals where the maximum shear stress is concentrated. In this case, the microstructure flows in accordance with an angle

that runs almost parallel to the diagonal, as shown in the image in Figure 3.

In spite of the apparent low degree of deformation in LSR (see Figure 3), the ferrite grains (light contrast) started to develop a substructure, as shown in Figure 4. Depending on the imaging mode applied, new ingrain boundaries (central part of the optical image in Figure 4(a) or different grey contrast (central part of the backscattered electron FEG-SEM image in Figure 4(b)) reveal such a subdivision of the original ferrite grains. The secondary electron images in Figures 4(c) and (d) clearly show that the break-up of the cementite lamellae into smaller plates has already started, albeit with a different intensity, depending on the pearlite colony.

The effect of the deformation on the ferrite microstructure is clearly illustrated when the EBSD images of the starting material in Figure 2 are compared to those in Figures 5(a) and (b), corresponding to the HSR of the sample deformed at 600 °C and 10 s⁻¹. The boundary density distribution per unit area as a function of the misorientation angle is shown in Figure 6(a), while number density for different boundary types is shown in Figure 6(b). Both figures clearly illustrate that deformation gives rise to a significant increase in LABs and also in HABs, albeit to a lesser extent. Additionally,

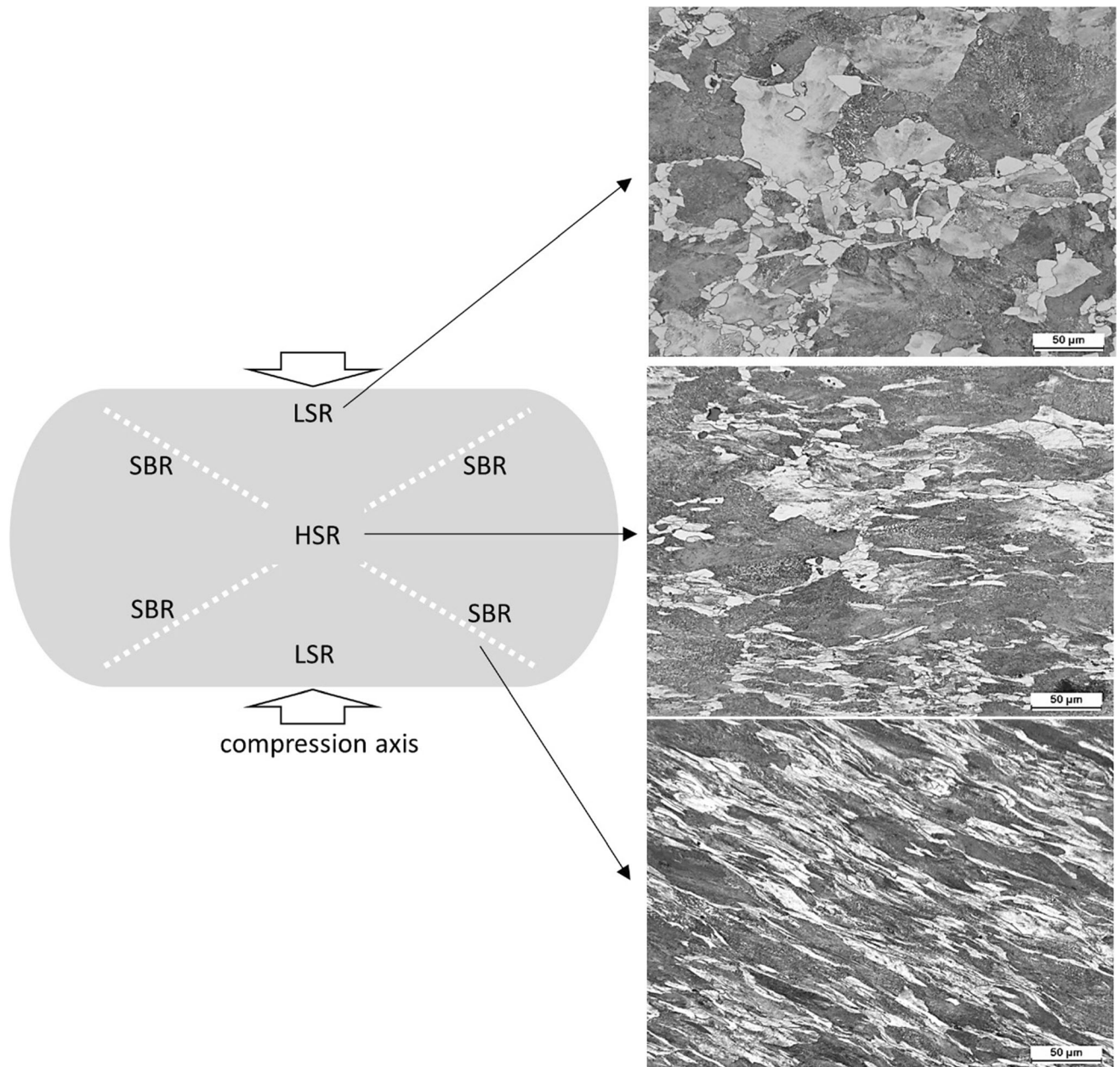


Fig. 3—Scheme showing the low strain region (LSR), high strain region (HSR) and shear band region (SBR), and the corresponding microstructures after deformation. SLR and HSR 700 °C and 10 s^{-1} and SBR 600 °C and 10 s^{-1} . True strain $\epsilon = 1$.

it would seem clear that, as the temperature decreases and strain rate increases, LAB density also increases.

Pearlite morphology was analysed in detail in both the HSR and the SBR. FEG-SEM micrographs in the central highly deformed region are shown in Figures 7(a) and (b). This figure illustrates the main characteristics of the pearlite in HSR. The microstructure comprises some islands of apparently unaffected lamellar pearlite and some areas where kinked lamellae appear, although the main part of the pearlite has evolved into a mixture of small ferrite crystallites and fully or partially globulised cementite. As shown in the high magnification FEG-SEM images in Figures 8(a)

and (b), different levels of globulisation appear as follows:

- Grooved cementite lamellae
- Plates of cementite showing a cellular type of microstructure
- Rows of cementite particles
- Discrete particles with different sizes and distribution (isolated, clustered)

Within the SBR, the degree of globulisation is significantly lower than in the HSR and most of the pearlite colonies remain, albeit with severe distortions, as can be seen in Figures 9(a) and (b). Kinking and shearing are the main mechanisms contributing to this

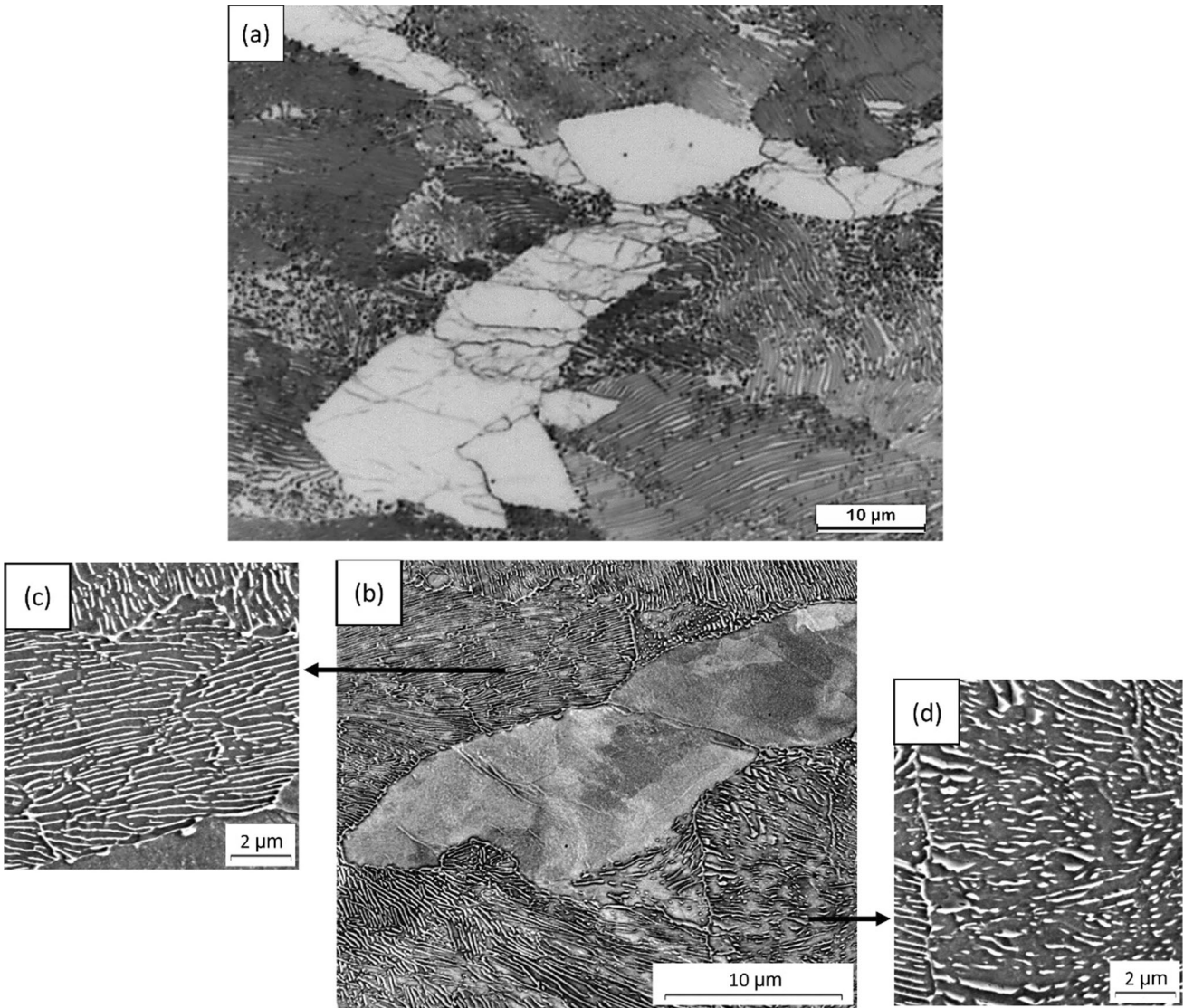


Fig. 4—Images from the LSR of the sample compressed at 700 °C and 10 s^{-1} (a) optical micrograph (b) backscattered FEG-SEM (central image) and (c) and (d) secondary electron FEG-SEM (lateral images) that show some details of the pearlite microstructure.

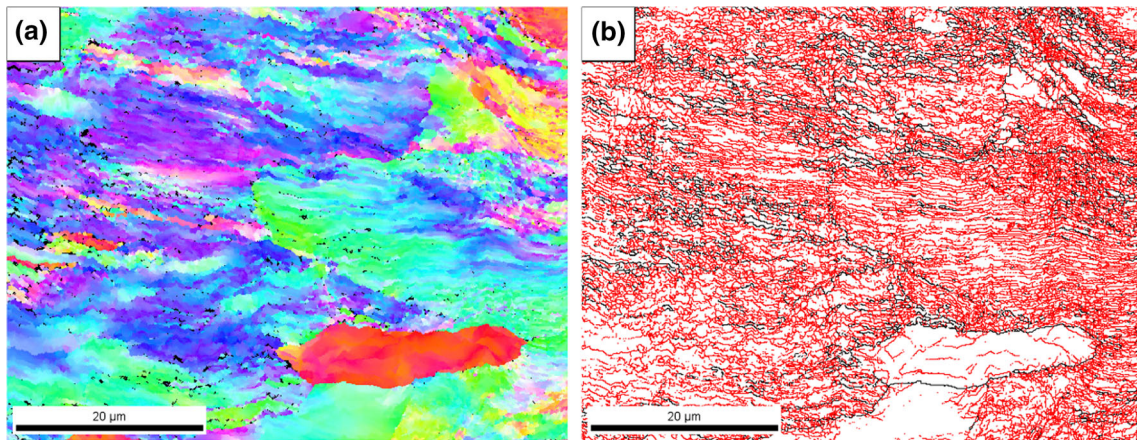


Fig. 5—EBSD images corresponding to (a) the orientation map (colour code as in Fig. 2(c)) and (b) low (red) and high (black) boundary map. Sample deformed at 600 °C and 10 s^{-1} (Color figure online).

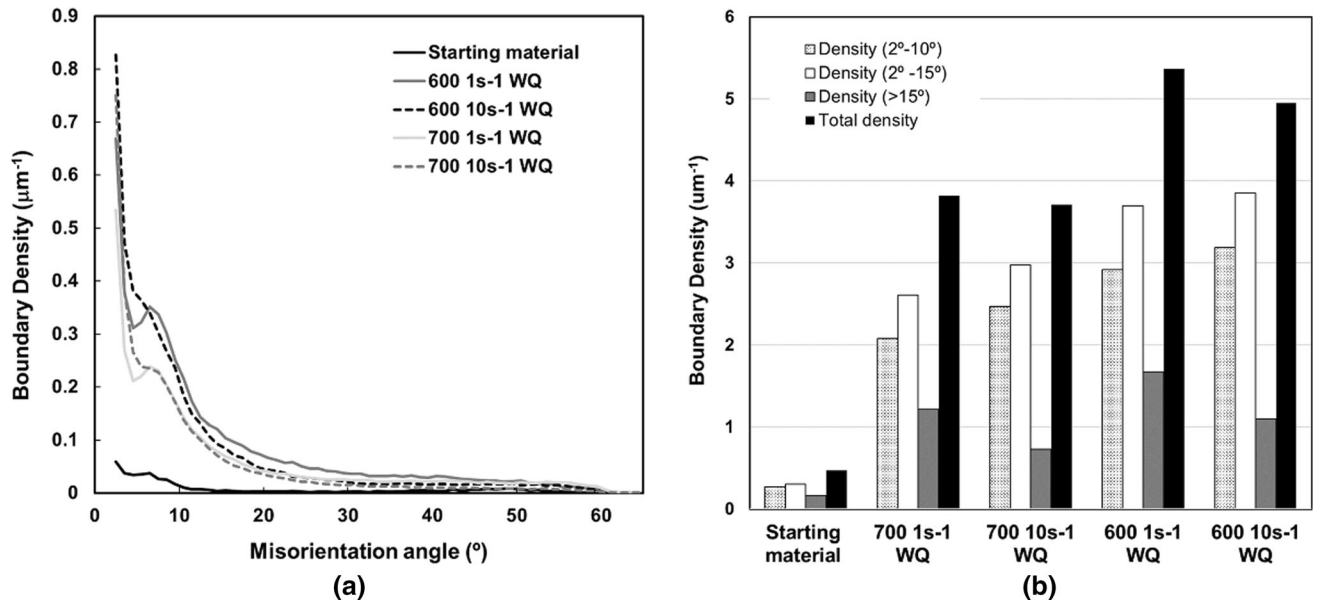


Fig. 6—(a) Distribution of the boundaries as a function of the misorientation angle and deformation conditions and (b) number density for different boundary types.

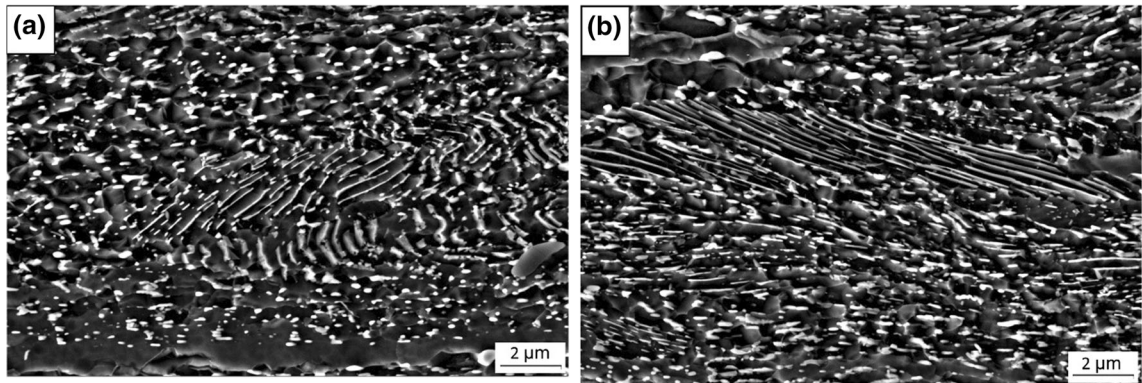


Fig. 7—FEG-SEM micrographs in HSR showing (a) kinked lamellae and fully globulised cementite, and (b) unaffected lamellar pearlite and partially globulised cementite. 700 $^\circ\text{C}$ 1 s^{-1} WQ.

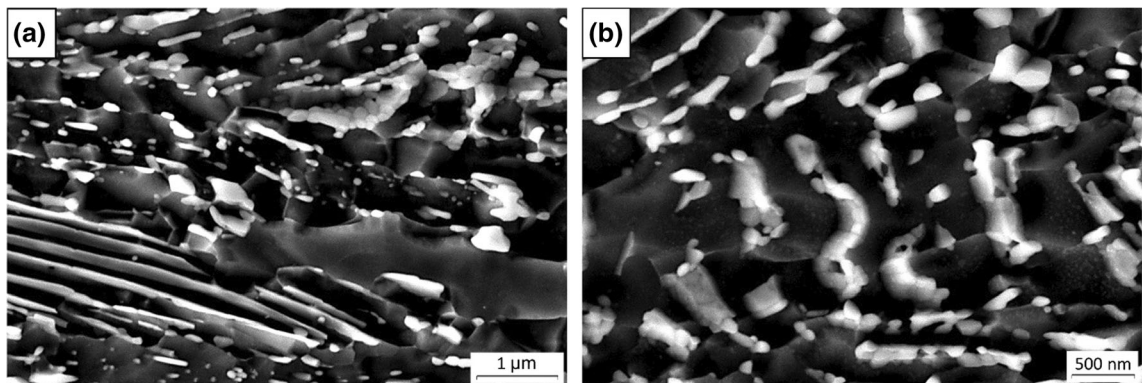


Fig. 8—FEG-SEM images at higher magnifications in HSR showing (a) plates of cementite showing a cellular type of microstructure and discrete particles, and (b) grooved lamellae and rows of cementite particles. 700 $^\circ\text{C}$ 1 s^{-1} WQ.

distortion of the pearlite. Their effect on the microstructure is more clearly illustrated in Figures 10(a) and (b).

The severe shearing in this region gives rise to kinking of the pearlite lamellae, and formation of small globular

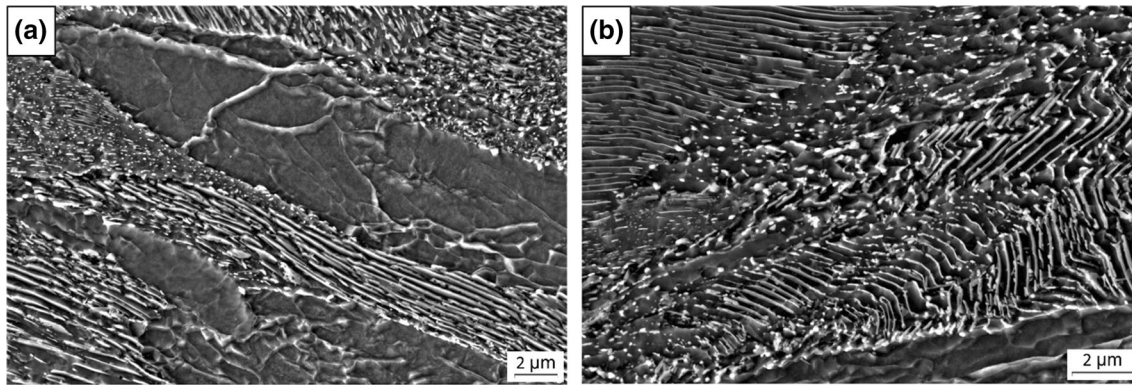


Fig. 9—FEG-SEM micrographs showing details of the pearlite morphology at upper (a) left and (b) right SBR. 700 °C 1 s⁻¹ WQ.

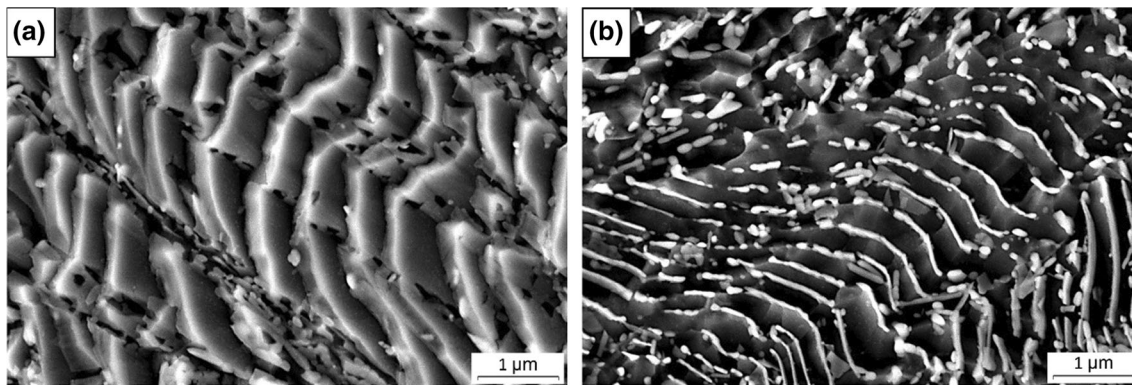


Fig. 10—FEG-SEM images at higher magnifications at upper (a) left and (b) right SBR. 700 °C 1 s⁻¹ WQ.

cementite can be clearly seen at the intersection between cementite and bands.

IV. DISCUSSION

As shown in Figure 1(b), the morphology of the cementite in pearlite that appears on the observation plane for the as-hot rolled bars is far from the ideal array of parallel and regularly separated cementite plates. Irregularities and discontinuities can be found within the same pearlite colony,^[19] which is a clear disadvantage when trying to outline the effect of deformation on cementite, particularly at early stages of deformation. However, although distribution of the deformation in the section of an axisymmetric compression specimen is usually far from being homogeneous,^[20] this can be an advantage for research purposes. Two distinct regions of the specimen were selected in order to research into the effect of the deformation applied on the cementite lamellae.

The first zone selected for observation of the pearlite corresponds to a region around one of the specimen diagonals (SBR) where shear stress induces the grains to elongate at an angle with respect to the stress applied. The inclination angle here is close to 40 deg, which enables a local shear strain of around 0.83 to be estimated.

Pearlite morphology in SBR regions is shown in Figures 9 and 10. Deformation in this area is highly heterogeneous at a local scale, leading to the formation of many shear bands. These bands contribute to the break-up of the lamellae as already reported by other authors.^[21] However, it has been observed that this phenomenon is quite local and takes place at the intersection between lamellae and shear bands. Outside these bands, the lamellae become kinked as can be seen in Figure 11(a), and develop a series of features, indicating that the cementite lamellae have started to dissolve or break. Subdivision of the pearlite into different units is evident in this figure. However, the phenomenon appears localised in the regions around the intersection of a shear band and the lamellae, while outside these highly deformed regions the lamellae appear more homogeneous in the FEG-SEM images. Partial dissolution of this cellular type of cementite microstructure is quite evident in Figure 11(b).

The second zone selected for pearlite observation corresponds to the central part of the specimen (HSR) where the microstructure appears elongated in the direction perpendicular to the stress applied. This zone corresponds approximately to the position of maximum radius caused by bulging of the specimen during deformation.^[22] The mean equivalent true strain across the section at maximum bulging position can be estimated at 1.1 by comparing the maximum diameter

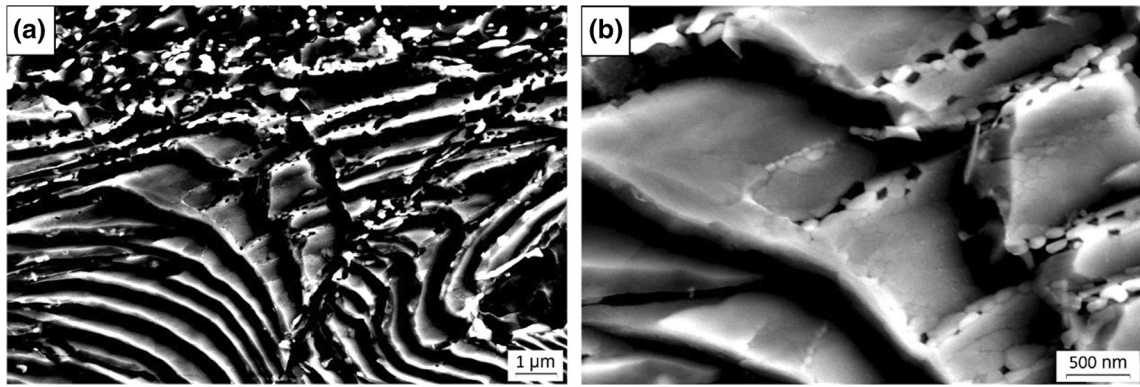


Fig. 11—Kinked cementite plates at the upper right SBR of the sample deformed at $700\text{ }^{\circ}\text{C}$ 1 s^{-1} : (a) general view and (b) close-up of the lamellae at higher magnifications, showing some regions of cellular cementite microstructure on the kinked plates.

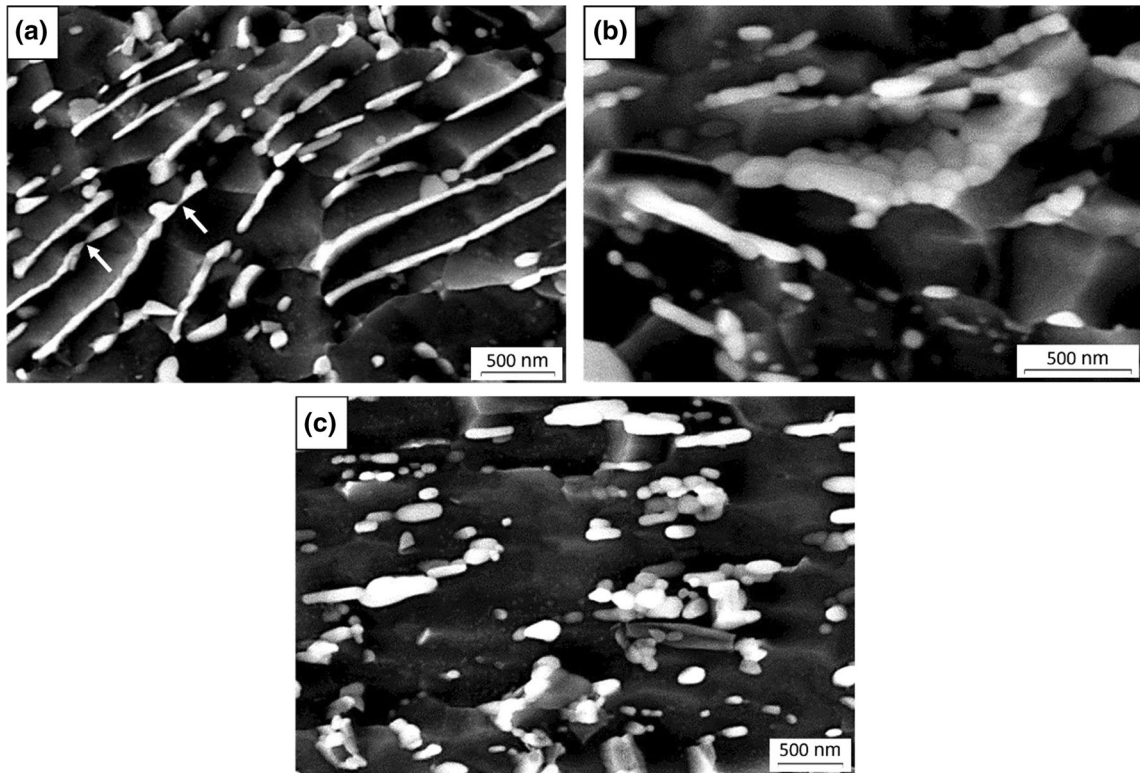


Fig. 12—Different cementite morphologies in the HSR (a) grooved lamellae, (b) cellular and (c) isolated particles and particle cementite. $700\text{ }^{\circ}\text{C}$ 1 s^{-1} WQ.

of the specimen before and after deformation. However, previous results, based on finite element modelling of compression tests, indicate that local strain at the centre of the specimen (HSR) may reach levels as high as 2 times that of nominal imposed strain.^[23,24] In such a case, this strain would seem sufficient to induce a dynamic spheroidisation mechanism of the cementite lamellae.^[8] The different stages of such a process taking place at $700\text{ }^{\circ}\text{C}$ and 1 s^{-1} are summarised in Figures 12(a) through (c). The first image (Figure 12(a)) shows an area of lamellar pearlite with clear indices of the first stages of globulisation, in which

the cementite plates are almost perpendicular to the observation plane and resemble strings on the images. At certain locations, some grooves appear on the cementite plate, leading to the formation of necks (see arrows) prior to the separation of cementite as globular particles.

Rastegari *et al.*^[8] suggested that dynamic spheroidisation of the cementite lamellae occurs as a result of the shearing of cementite platelets followed by penetration of the ferrite, so as to complete fragmentation and subsequent rounding. TEM work on hot deformed pearlite^[17,18] has revealed the presence of dislocations in

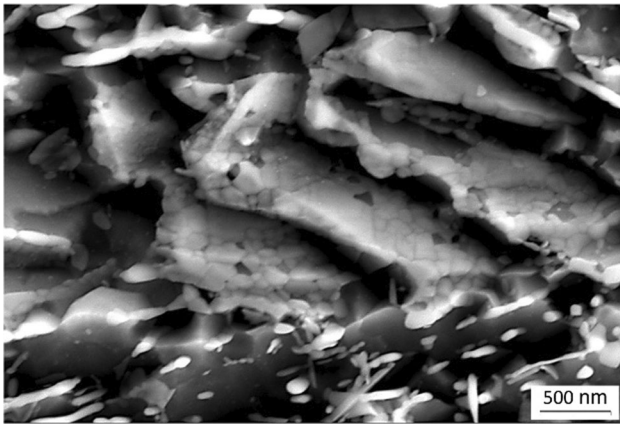


Fig. 13—Cellular cementite microstructure after deformation at 600 °C 1 s⁻¹ and WQ.

ferrite and at the interphase, and sub-boundaries were also seen in cementite in Reference 18. These sub-boundaries were assumed to extend during plastic deformation, leading to the formation of grooves that, due to their high curvature, induce local dissolution of the cementite, thus contributing to break-up of the lamellae. The image in Figure 12(b) of a few inclined cementite plates with respect to the observation plane shows that the lamellae have transformed into a complete pattern of crystallites with sizes ranging from about 50 up to around 300 nm. These crystallites form a single layer on the cementite plate thickness and appear almost equiaxed. For its part, the lateral image of a plate almost perpendicular to the observation plane takes on the typical appearance of a row of semi-globulised cementite particles like those shown in Figure 12(a).

The mechanisms activated at 600 °C and 1 s⁻¹ are similar to those illustrated in Figure 12. The subdivision of the cementite lamellae into a series of crystallites is exclusive to the warm deformed samples, although this appears irrespective of the deformation being applied at 700 °C or at 600 °C. As shown in Figure 13, the subdivided or cellular cementite is also present in the sample deformed at 600 °C and 1 s⁻¹. At some points of the lamellae, dark contrast crystallites can be observed, which were identified as ferrite. The image in Figure 14 shows more clearly how the ferrite phase penetrates the pattern formed by the cementite crystallites (see arrows), confirming that dissolution of this phase during deformation is an important mechanism leading to the break-up of plates and subsequent globulisation.

A close analysis of the pearlite was conducted using EBSD in this HSR. Figures 15(a) through (c) show EBSD patterns taken from a single lamella in positions distanced at 1 μm. In this case, the lamella evidences straight geometry, although even so, it is possible to detect its rotation, with misorientation between both positions being approximately 3.4 deg. This rotation, therefore, seems to be induced by the deformation applied, and is very likely to be related to subdivision of the pearlite into different units that ultimately facilitate its spheroidisation. Orientation gradients of the pearlite have been already reported by other authors.^[25] In the

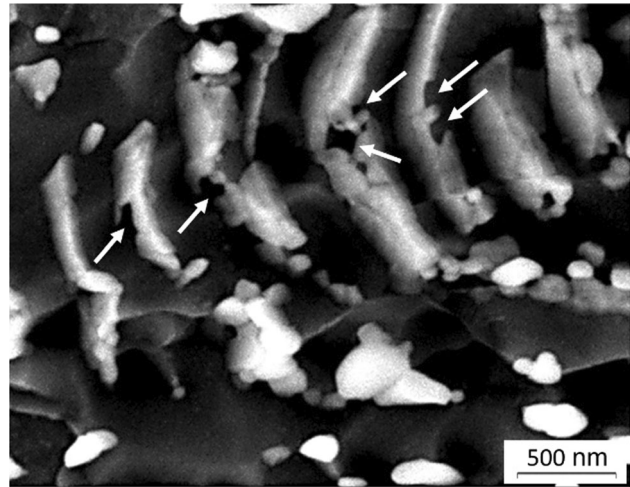


Fig. 14—Close-up of ferrite protrusion in the cementite lamellae and formation of cementite clusters and individual particles. 700 °C 1 s⁻¹ WQ.

referred work those orientation gradients are related to the curvature developed in some lamellae during austenite to ferrite-pearlite transformation. The results obtained in the present work are in line with those obtained by Tao *et al.*^[18] who defend the sub-boundary generation as being necessary for groove formation and final dissolution of the cementite.

At the same time as the phenomena described take place in the pearlite, major changes also occur in the ferrite matrix. Heterogeneities in the microstructure regarding pearlite and ferrite regions influence activation of different softening mechanisms in the different areas. The evolution of both ferrite and pearlite regions were examined using EBSD in combination with FEG-SEM images. Figure 16 shows HABs (in black trace) over the IQ map within which different zones are identified, numbered F1 and F2 in the case of proeutectoid ferrite and FP1 to FP5 in that of pearlite. FEG-SEM cropped images for these zones are shown in Figures 17 through 19, along with the respective low (traced in red) and high (traced in black) angle boundary maps, and with the corresponding point-to-point and point-to-origin profiles. The combination of the different images provides a general overview of local microstructural evolution as follows: the FEG-SEM images made it easier to draw a distinction between phases (ferrite and pearlite) and the degree of cementite spheroidisation, while the EBSD images and profiles enabled the local grain boundary character to be determined and the actuating mechanism inferred.

A. Proeutectoid Ferrite

In the proeutectoid ferrite regions, evolution of the microstructure with deformation can mainly lead to two different states. The first, characterised by the microstructure referred to as F1 (Figure 17(a)), is related to strain accumulation along the grain. The point-to-origin profile in Figure 17(c) shows the continuous increase in misorientation along the deformed

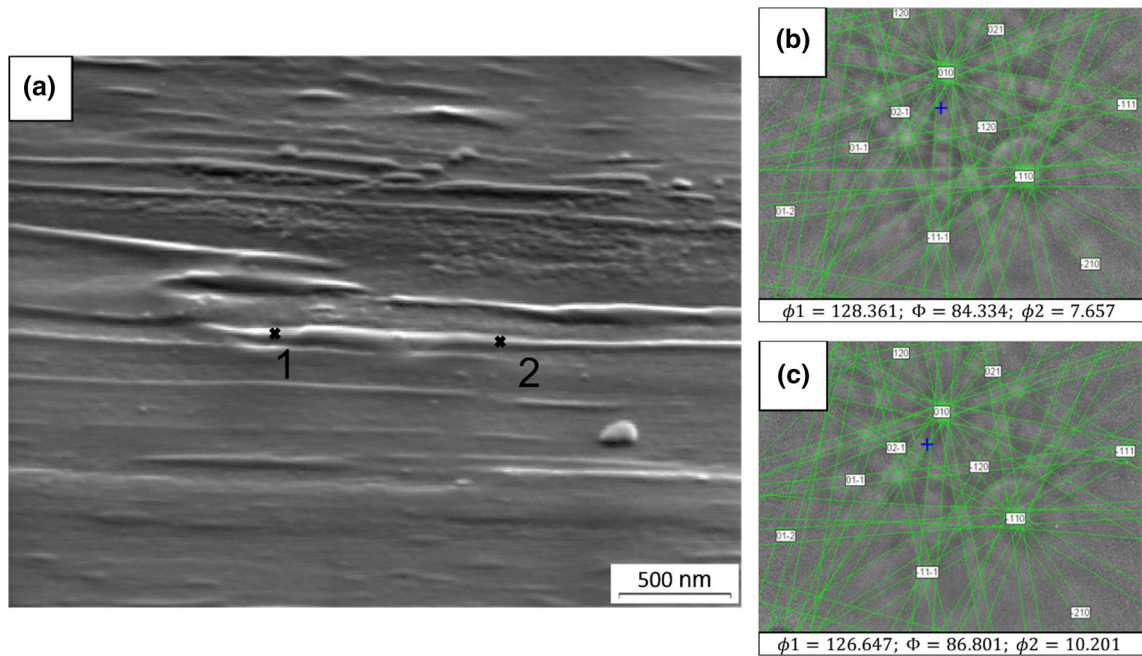


Fig. 15—(a) Close-up of the lamellae studied using EBSD. EBSD patterns obtained at positions (b) 1 and (c) 2, respectively.

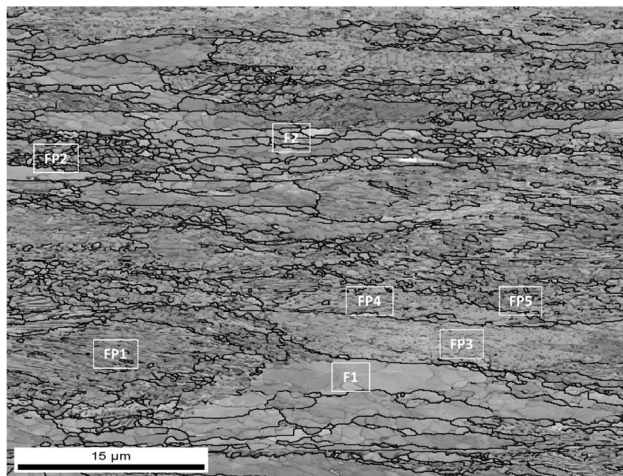


Fig. 16—EBSD image corresponding to the high angle boundary map (black) over the IQ map. 700 °C 1 s⁻¹ WQ.

grain in the rolling direction (up to 10 deg at a 15 μm distance, approximately), which leads to the beginning of LAB formation (misorientation near 1 deg) due to dislocation arrangement, as shown in the point-to-point misorientation profile in the same figure.

A second state is represented by the microstructure referred to as F2 in Figure 17(b). The FEG-SEM image and grain boundary map show the development of LABs in the highly elongated ferrite grains parallel to the rolling direction. The point-to-point profile in Figure 17(c) has revealed that these boundaries have developed higher misorientation angles (between 5 and 13 deg) than those referred to in F1. Additionally, the formation of new HABs is also observed in the same figure. These new grains define misorientations up to 61 deg, the enclosed crystallite size being between 0.2

and 2.3 μm . From the behaviour observed, it could be concluded that the warm deformed proeutectoid ferrite evolves during the thermomechanical sequence applied, with recovery being the main softening process observed in line with expected behaviour due to its high stacking fault energy. Subsequent recrystallisation does also occur, albeit to a lesser extent: a continuous dynamic recrystallisation, as a result of dislocation accumulation at the LABs or due to a subgrain rotation mechanism, is believed to occur in some zones for the applied deformation.

The result of activating these two mechanisms in the microstructure is that in the area of proeutectoid ferrite, rearrangement of dislocations due to recovery gives rise to the formation of LABs. The proportion of HABs being created by recrystallisation is lower.

B. Pearlite

In the pearlite regions, activation of softening mechanisms was noted to have been influenced by the dynamic spheroidisation of the cementite lamellae, as argued previously by different authors,^[13,16] which leads to a wider variety of microstructural stages as explained below. Additionally, the entire spheroidisation process during plastic deformation involving the break-up of lamellae into fragments followed by the rounding off of those fragments has been observed to occur gradually and locally at different grades, as also explained below.

Figure 18(a) shows a region where the pearlite, although deformed, maintains its initial lamellar morphology, being referred to as FP1. The point-to-origin misorientation profile in the ferrite along the pearlite colony shows a continuous increase in misorientation up to 17 deg within 9 μm (Figure 18(c)). The grain boundary map shows a high density of low angle

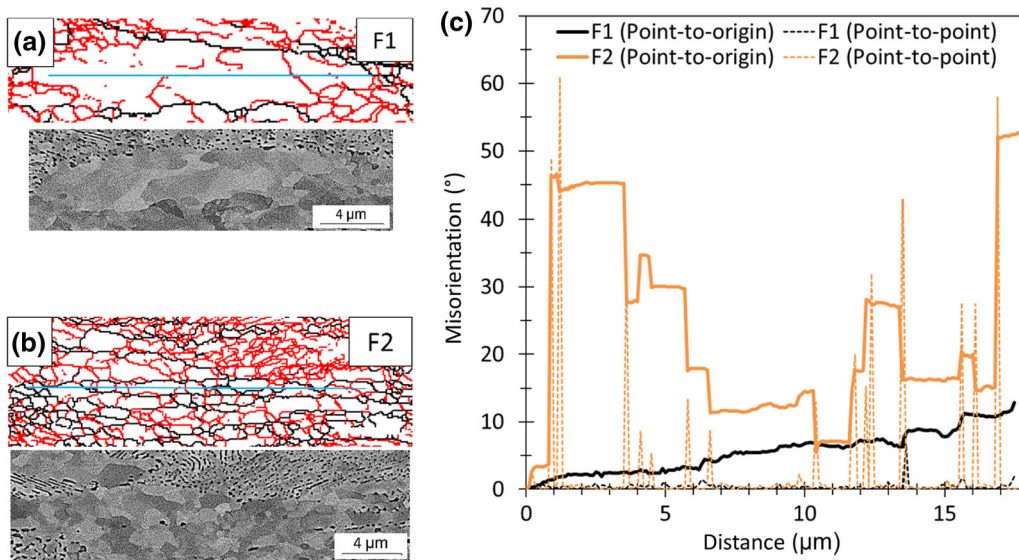


Fig. 17—FEG-SEM cropped images, along with the respective low (red) and high (black) angle boundary maps for (a) F1 and (b) F2 regions, and (c) corresponding point-to-origin and point-to-point profiles (Color figure online).

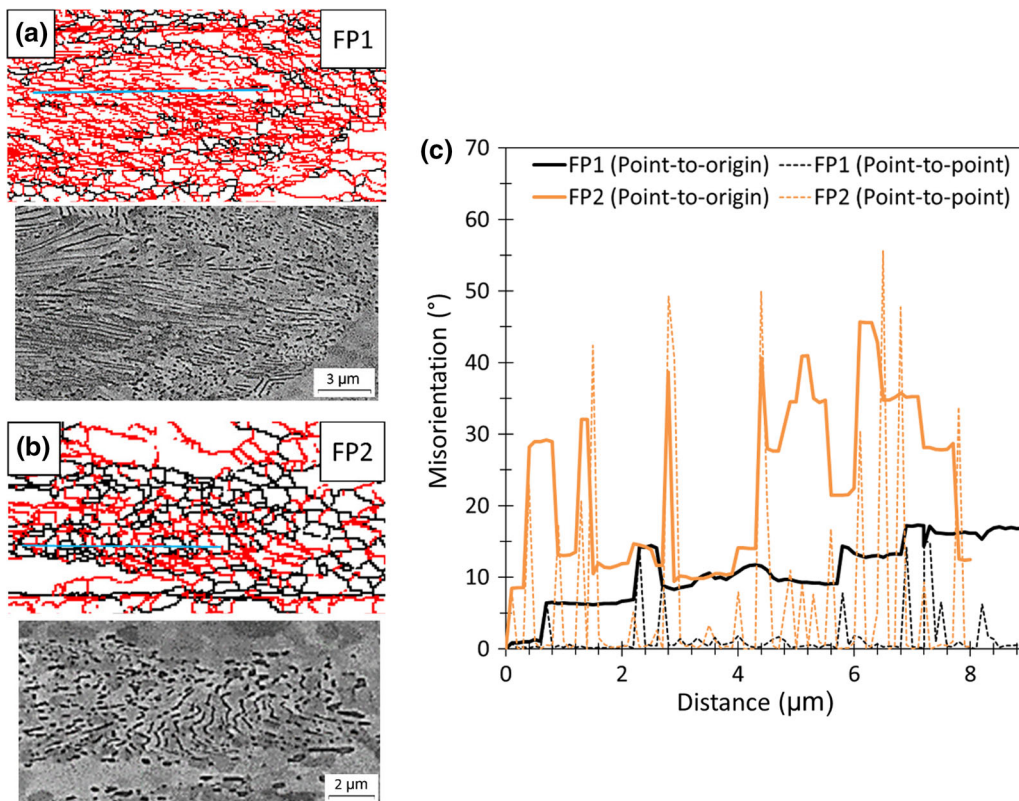


Fig. 18—FEG-SEM cropped images, along with the respective low (red) and high (black) angle boundary maps for (a) FP1 and (b) FP2 regions, and (c) corresponding point-to-origin and point-to-point profiles (Color figure online).

boundaries with misorientations ranging from 1 to 14 deg as observed in the point-to-point misorientation profile.

Distortion and dissolution of the pearlite lamellae is evident in other pearlite region, referred to as FP2 (Figure 18(b)). In this region, point-to-point and

point-to-origin misorientation profiles in Figure 18(c), show that these changes in morphology might facilitate the formation of new LABs in ferrite (ranging from 3 to 11 deg) and mainly HABs, up to 56 deg, leading to an equiaxed subgrain/grain size of between 0.1 and 1.2 μm .

An alternating point-to-origin misorientation profile evolves within this region.

In Figure 19(a), dynamic spheroidisation has taken place in the pearlite lamellae. In this case, referred to as FP3, it is possible to observe strain accumulation along the analysed grain. The point-to-origin profile in Figure 19(d) shows the continuous increase in misorientation (up to 14 deg at a 9 μm distance) along the deformed grain in the rolling direction, which leads to the formation of LABs (misorientation ranging from 1 to 3 deg) as shown in the point-to-point profile in the same figure. In this case, with the presence of fine cementite particles due to spheroidisation, the softening of ferrite in the areas of the former pearlite colonies would seem to be retarded and the formation of subgrains in ferrite is not complete, this probably being related to the pinning effect exerted by the fine cementite particles.

In Figure 19(b), dynamic spheroidisation has also taken place in the pearlite lamellae. Nonetheless, in this case, referred to as FP4, it is possible to observe the formation of ferrite subgrains. Recovery and the subsequent subgrain structure would seem to develop more easily in these areas where cementite is highly spheroidised but is coarser than in the previous case. Equiaxed subgrains can be observed on the boundary map, with sizes of between 0.2 and 1.6 μm , with particle spacing possibly determining subgrain size. The point-to-point misorientation profile in Figure 19(d), does not exceed 15 deg, being in the range of 2 to 14 deg, and the accumulative type of point-to-origin misorientation

profile is no longer observed. Instead, an orientation alternating misorientation profile evolves. In this case, the migration of LABs for subgrain formation in the well-known recovery process seems to be facilitated by cementite lamellae break-up and dissolution. The morphological changes in the cementite itself should be encouraged *via* the migration of defects in the cementite lamellae and the break-up related to Rayleigh instability phenomena.

Another fully spheroidised pearlite region is shown in Figure 19(c). In this case, referred to as FP5, a very fine and equiaxed substructure was developed ($< 1 \mu\text{m}$). The point-to-point profile in Figure 19(d) shows that higher misorientation is built up in ferrite within the subgrain microstructure with respect to that found in FP4, along with an alternating point-to-origin profile also showing higher misorientations. In addition, some grains surrounded by HABs are readily observed, with misorientation angles of up to 24 deg and sizes of between 0.1 and 0.6 μm . Continuous dynamic recrystallisation is thought to be behind the behaviour observed. At this stage, this phenomenon along with the presence of fine carbides that suppress discontinuous recrystallisation would seem to facilitate the gradual formation of subgrains that eventually become grains surrounded by HABs, giving rise to the evolution of a more equiaxed grain shape. This mechanism, which could also be referred to as continuous recrystallisation, would seem to prevail over the discontinuous one. This result is in line with that previously reported by Song *et al.*^[16] Additionally, certain degree of plastic strain partitioning

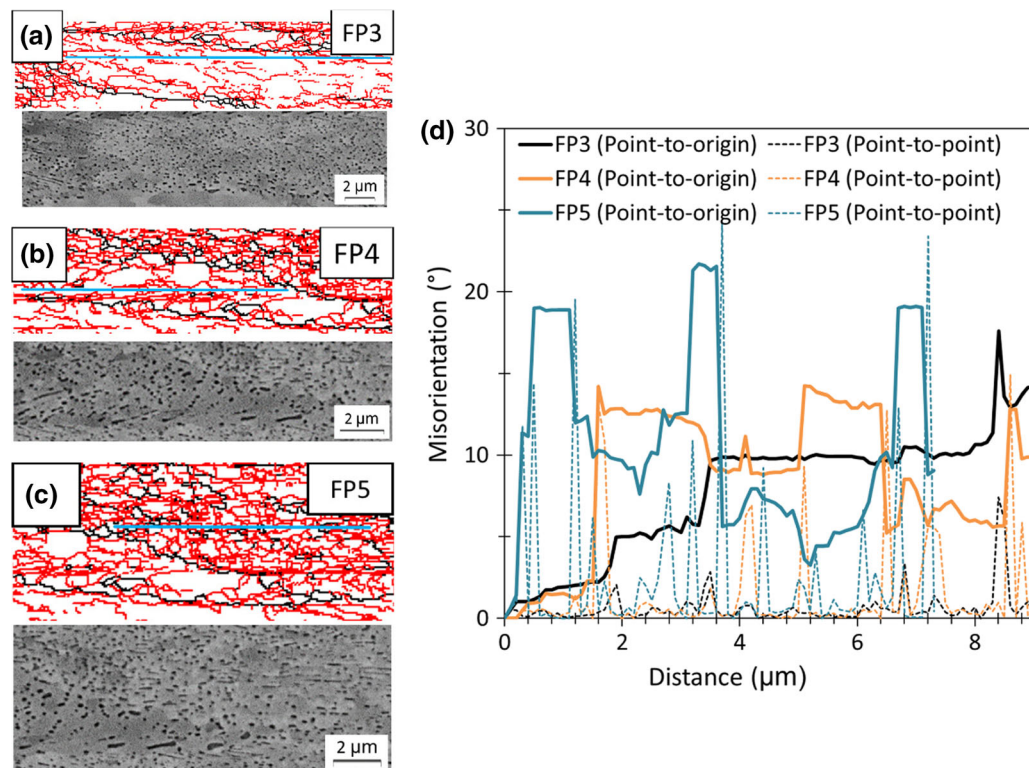


Fig. 19—FEG-SEM cropped images, along with the respective low (red) and high (black) angle boundary maps for (a) FP3, (b) FP4 and (c) FP5 regions, and (d) corresponding point-to-origin and point-to-point profiles (Color figure online).

between ferrite grains and pearlite colonies, and between ferrite and cementite lamellae inside pearlite is expected. Referred to pearlite, the ferrite-cementite strain partitioning and localisation is also known to depend on the morphology and distribution of ferrite grains and pearlite colonies. As a consequence, as it has been shown, some regions seem to develop higher local deformation and facilitate the CDRX: after a strain hardening limited by dynamic recovery and once a critical dislocation density is reached, a new grain boundary stable configuration is formed.

As shown in Figure 6(a) and (b), the application of warm deformation gives rise to a clear increase in the density per unit length of all the boundaries. The plot in Figure 6(a) clearly shows that the density of these LABs increases far more than that corresponding to the HABs. Moreover, LAB density increases systematically as deformation temperature (T) decreases and the strain rate, $\dot{\epsilon}$, rises, which would seem to indicate some correlation with the Zener–Hollomon parameter, and, consequently, with the stress. The constitutive equations reported for warm deformation of ferrite^[26] and pearlite^[27] were used to research into the relation between boundary density and steady state stress, σ_{ss} , in the case of each of these two microstructural

constituents. According to the formulation proposed in Reference 28:

$$\sigma_{ssi} = \frac{1}{\alpha_i} \operatorname{arcsinh} \left(\frac{Z_i}{A_i} \right)^{1/n_i} \quad [1]$$

where Z is the Zener–Hollomon parameter defined as $Z_i = \dot{\epsilon} \exp(\frac{Q_i}{RT})$, α , A , n are the material constants, Q is the activation energy for deformation, R is the gas constant, $\dot{\epsilon}$ is the strain rate and T is the absolute temperature. The i subscript indicates ferrite or pearlite, and the corresponding constants are those reported in literature,^[26,27] as shown in Table II. The activation energy proposed for ferrite,^[26] is quite large and seems to be the result of the use in this work of a value of n which is also quite large. That is why these values have been considered apparent here and have been applied only to estimate the stress in each phase, although it is clear they cannot be used to estimate active deformation mechanisms. As shown in Figure 20, there is a linear dependence between LAB density and estimated stress in the case of ferrite or pearlite. Additionally, the same figure shows that application of this formulation leads to a linear relation between the estimated steady state stress of the pearlite and that of the ferrite in the case of the pair of values corresponding to the same deformation temperature and strain rate. That is why a linear relation remains, irrespective of whether ferrite or pearlite is being taken into consideration, although it is a clear indication that the new boundaries will have formed dynamically during deformation. An increase in density of HAB density with deformation is also noticeable, although this is almost irrespective of the temperature and strain rate applied.

Table II. Constitutive Equation Parameters for Ferrite and Pearlite Warm Deformation

Parameters	Ferrite ^[26]	Pearlite* ^[27]
A_i (s^{-1})	2.0×10^{33}	2.8×10^{22}
Q_i (kJ/mol)	630.82	423.63
n_i	10.78	7.58
α_i (MPa^{-1})	0.0036	0.0028

*at $\epsilon = 0.4$.

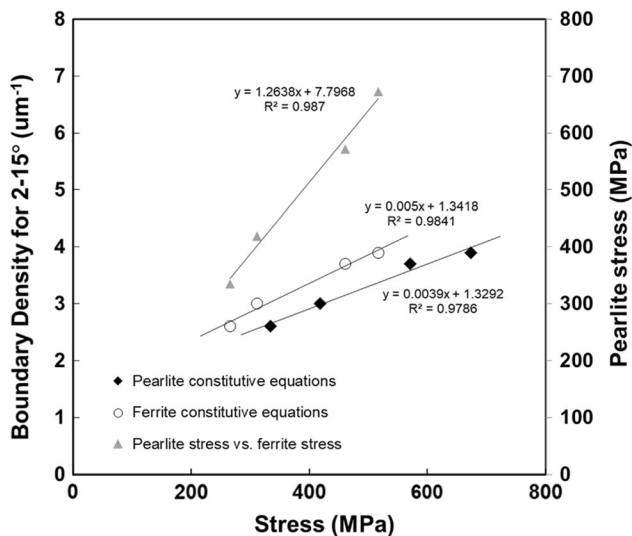


Fig. 20—Relation between LAB density and estimated stress obtained by applying constitutive equations reported for warm deformation of ferrite and pearlite.

V. CONCLUSIONS

Research was conducted into the effect of the temperature and strain rate on the pearlite spheroidisation process and ferrite microstructure refinement through dynamic recovery and continuous dynamic recrystallisation, with the following conclusions being drawn:

1. Different stages of the pearlite globulisation process may be observed (grooved and cellular lamellae and isolated cementite particles). When grooves appear on the cementite plate, necks start to form prior to the separation of cementite as globular particles. In some regions, it is possible to observe the lamellae transformed into a complete pattern of crystallites. The ferrite phase penetrates at some points in the pattern formed by the cementite crystallites, indicating that dissolution of this phase during deformation is an important mechanism, which leads to the break-up of plates and subsequent globulisation.
2. Ferrite softening during HWD may be attributed to dynamic recovery and continuous dynamic recrystallisation, although the evolution of this phase depends to a great extent on the region subject to study. In pearlite regions, evolution of the ferrite

microstructure is greatly influenced by the degree of dynamic spheroidisation of the cementite lamellae. The fine cementite particles exert a major dragging force on the migration of grain boundaries due to Zener pinning, which can lead to a very fine-grained microstructure. The softening mechanisms are nevertheless the same within the proeutectoid ferrite and pearlitic ferrite.

3. The LAB density increase in the ferrite correlates with the Zener–Hollomon parameter. When applying the constitutive equations for warm deformation of ferrite and pearlite, it was found that there is a linear relation between the density of low angle boundaries and the steady-state stress estimated for pearlite or proeutectoid ferrite, indicating that the new boundaries will have been formed dynamically during deformation.
4. HAB density also increases with deformation, albeit almost irrespective of the temperature and strain rate applied. The continuous dynamic recrystallisation mechanism seems to contribute to the formation of high angle boundaries.

ACKNOWLEDGMENTS

The authors express their gratitude for the financial support of the European Coal and Steel Community. RFCS-2015. Project Number: 709828

CONFLICT OF INTEREST

On behalf of all authors, the corresponding author states that there is no conflict of interest.

FUNDING

Open Access funding provided thanks to the CRUE-CSIC agreement with Springer Nature.

OPEN ACCESS

This article is licensed under a Creative Commons Attribution 4.0 International License, which permits use, sharing, adaptation, distribution and reproduction in any medium or format, as long as you give appropriate credit to the original author(s) and the source, provide a link to the Creative Commons licence, and indicate if changes were made. The images or other third party material in this article are included in the article's Creative Commons licence, unless indicated otherwise in a credit line to the material. If material is not included in the article's Creative Commons licence and your intended use is not permitted by statutory

regulation or exceeds the permitted use, you will need to obtain permission directly from the copyright holder. To view a copy of this licence, visit <http://creativecommons.org/licenses/by/4.0/>.

REFERENCES

1. V.V. Basabe, J.J. Jonas, and C. Ghosh: *Adv. Mater. Res.*, 2011, vol. 409, pp. 829–34.
2. Y. Fu, H. Yu, and P. Tao: *Int. J. Miner. Metall. Mater.*, 2014, vol. 21, pp. 26–35.
3. N.N. Jia, K. Guo, Y.M. He, Y.H. Wang, J.G. Peng, and T.S. Wang: *Mater. Sci. Eng. A.*, 2017, vol. 700, pp. 175–82.
4. M. Caruso, H. Verboomen, and S. Godet: *Adv. Mater. Res.*, 2011, vol. 409, pp. 666–71.
5. H. Dong, X. Sun, W. Hui, S. Zhang, J. Shi, and M. Wang: *ISIJ Int.*, 2008, vol. 48, pp. 1126–32.
6. J. Arruabarrena, B. López, and J.M. Rodríguez-Ibabe: *Metall. Mater. Trans. A.*, 2016, vol. 47A, pp. 412–23.
7. J. Arruabarrena, B. López, and J.M. Rodríguez-Ibabe: *Metall. Mater. Trans. A.*, 2014, vol. 45A, pp. 1470–84.
8. H. Rastegari, A. Kermanpur, A. Najafizadeh, D. Porter, and M. Somani: *J. Alloys Compd.*, 2015, vol. 626, pp. 136–44.
9. C. Prasad, P. Bhuyan, C. Kaithwas, R. Saha, and S. Mandal: *Mater. Des.*, 2018, vol. 139, pp. 324–35.
10. K. Handa, Y. Kimura, Y. Yasumoto, T. Kamioka, and Y. Mishima: *Mater. Sci. Eng. A.*, 2010, vol. 527, pp. 1926–32.
11. M.-C. Zhao, T. Hanamura, H. Qiu, and K. Yang: *Metall. Mater. Trans. A.*, 2006, vol. 37A, pp. 1657–64.
12. M.-C. Zhao, T. Hanamura, F. Yin, H. Qiu, and K. Nagai: *Metall. Mater. Trans. A.*, 2008, vol. 39A, pp. 1691–701.
13. L. Storójeva, D. Ponge, R. Kaspar, and D. Raabe: *Acta Mater.*, 2004, vol. 52, pp. 2209–20.
14. M.L. Martínez-Pérez, C.R. Borlado, F.J. Mompeán, M. García-Hernández, J. Gil-Sevillano, J. Ruiz-Hervías, J.M. Atienza, M. Elices, R.L. Peng, and M.R. Daymond: *Acta Mater.*, 2005, vol. 53, pp. 4415–25.
15. M. Umemoto, Y. Todaka, and K. Tsuchiya: *Mater. Sci. Forum.*, 2003, vol. 426–432, pp. 859–64.
16. R. Song, D. Ponge, D. Raabe, and R. Kaspar: *Acta Mater.*, 2005, vol. 53, pp. 845–58.
17. S. Chattopadhyay and C.M. Sellars: *Acta Metall.*, 1982, vol. 30, pp. 157–70.
18. T. Wu, M. Wang, Y. Gao, X. Li, Y. Zhao, and Q. Zou: *J. Iron Steel Res. Int.*, 2012, vol. 19, pp. 60–66.
19. F. Frank and K. Puttick: *Acta Metall.*, 1956, vol. 4, pp. 206–10.
20. R.W. Evans and P.J. Scharning: *Mater. Sci. Technol.*, 2002, vol. 18, pp. 1389–98.
21. M.W. Kapp, A. Hohenwarter, S. Wurster, B. Yang, and R. Pippan: *Acta Mater.*, 2016, vol. 106, pp. 239–48.
22. X. Wang, H. Li, K. Chandrashekhara, S.A. Rummel, S. Lekakh, D.C. Van Aken, and R.J. O'Malley: *J. Mater. Process. Technol.*, 2017, vol. 243, pp. 465–73.
23. P. Uranga, I. Gutiérrez, and B. López: *Mater. Sci. Eng. A.*, 2013, vol. 578, pp. 174–80.
24. C.J. Bennett, S.B. Leen, E.J. Williams, P.H. Shipway, and T.H. Hyde: *Comput. Mater. Sci.*, 2010, vol. 50, pp. 125–37.
25. T. Takahashi, D. Ponge, and D. Raabe: *Steel Res. Int.*, 2007, vol. 78, pp. 38–44.
26. D. Wang, J. Jin, and X. Wang: *J. Mater. Process. Technol.*, 2017, vol. 245, pp. 80–90.
27. H. Rastegari, M. Rakhshkhorshid, M.C. Somani, and D.A. Porter: *J. Mater. Eng. Perform.*, 2017, vol. 26, pp. 2170–78.
28. J.J. Jonas, C.M. Sellars, and W.J.M.M. Tegart: *Metall. Rev.*, 1969, vol. 14, pp. 1–24.

Publisher's Note Springer Nature remains neutral with regard to jurisdictional claims in published maps and institutional affiliations.